Available online at www.sciencedirect.com
SCIENCE DIRECT®
Journal of Computational Physics 207 (2005) 542–567
JOURNAL OF COMPUTATIONAL PHYSICS
www.elsevier.com/locate/jcp

Mapped weighted essentially non-oscillatory schemes: Achieving optimal order near critical points ☆

Andrew K. Henrick [a], Tariq D. Aslam [b,*], Joseph M. Powers [a]

[a] *Department of Aerospace and Mechanical Engineering, University of Notre Dame, Notre Dame, IN 46556-5637, USA*
[b] *MS P952, Dynamic Experimentation Division, Los Alamos National Laboratory, Los Alamos, NM 87545, USA*

Received 10 September 2004; received in revised form 28 January 2005; accepted 28 January 2005
Available online 17 March 2005

Abstract

In this paper, a new fifth-order weighted essentially non-oscillatory scheme is developed. Necessary and sufficient conditions on the weights for fifth-order convergence are derived; one more condition than previously published is found. A detailed analysis reveals that the version of this scheme implemented by Jiang and Shu [G.-S. Jiang, C.-W. Shu, Efficient implementation of weighted ENO schemes, J. Comput. Phys. 126 (1996) 202–228] is, in general, only third-order accurate at critical points. This result is verified in a simple example. The magnitude of ϵ, a parameter which keeps the weights bounded, and the level of grid resolution are shown to determine the order of the scheme in a non-trivial way. A simple modification of the original scheme is found to be sufficient to give optimal order convergence even near critical points. This is demonstrated using the one-dimensional linear advection equation. Also, four examples utilizing the compressible Euler equations are used to demonstrate the scheme's improved behavior for practical shock capturing problems.

Keywords: WENO; Hyperbolic equations

1. Introduction

Weighted essentially non-oscillatory (WENO) finite difference schemes have become one of the most popular methods for approximating solutions to hyperbolic conservation equations. In this paper, the fifth-order WENO method is analyzed using a simple one-dimensional model problem given by

☆ This study has been supported by Los Alamos National Laboratory and performed under the auspices of the US Department of Energy.
* Corresponding author. Tel.: +1 505 667 1367; fax: +1 505 667 6372.
E-mail addresses: ahenrick@nd.edu (A.K. Henrick), aslam@lanl.gov (T.D. Aslam), powers@nd.edu (J.M. Powers).

0021-9991/$ - see front matter © 2005 Published by Elsevier Inc.
doi:10.1016/j.jcp.2005.01.023

$$\frac{\partial u}{\partial t}+\frac{\partial f}{\partial x}=0, \tag{1}$$

where $u(x, t)$ is a conserved quantity, $f(u(x, t))$ describes its flux, and x and t denote space and time, respectively. In general, the domain $t \in [0, \infty)$ and $x \in [x_0, x_N]$ is considered. The results found by examination of this model problem can be generalized for systems of higher dimension.

Hyperbolic problems characterized by Eq. (1) admit discontinuous solutions. Such discontinuities introduce spurious oscillations in the approximate solutions generated by many traditional numerical methods. In order to address this issue, total-variation diminishing (TVD) schemes were developed in [2], founded on the work of Van Leer [3,4]. Later, Harten et al. [5] introduced essentially non-oscillatory (ENO) schemes. Instead of using a single fixed stencil to approximate spatial fluxes, an rth order ENO scheme uses a set of r candidate stencils. An indicator of smoothness of the solution is determined over each stencil. The stencil over which the solution is smoothest is then chosen in an attempt to diminish the effect of a discontinuity on neighboring cells. This method was further developed by Shu and Osher [6,7] who introduced pointwise ENO schemes which involve significantly fewer computations for multidimensional problems with inhomogeneous source terms than their cell-averaged counterparts.

Subsequently, Liu et al. [8] introduced WENO schemes, again using a cell-averaged approach. In such schemes, spatial derivatives are calculated using a convex combination of the numerical fluxes associated with each candidate stencil. This is accomplished by weighting the contribution of each flux according to the smoothness of the solution over each stencil. Using the indicator of smoothness introduced by Liu et al., an rth order ENO scheme can be converted into an $(r + 1)$th order WENO scheme. Suggesting a new indicator of smoothness, Jiang and Shu [1] then developed WENO5, a pointwise WENO scheme. WENO5 converges at fifth order in special cases and is differentiated from other fifth-order WENO schemes by the weights used in [1]. Balsara and Shu [9] showed that a $(2r - 1)$th order WENO scheme can be constructed from the stencils of an rth order ENO scheme for $r = 4$, 5, 6 and 7. Also, Fedkiw and co-workers [10,11] have noted that ϵ, a parameter in these schemes which introduces a numerical bound on the weights, is a dimensional quantity and have suggested an appropriate scaling.

Despite the fifth-order convergence behavior often exhibited by WENO5, its actual rate of convergence is less than fifth order for many problems. In fact, the analysis done in [1] does not identify all the properties of the weights which are necessary for a WENO scheme to converge at fifth-order. Furthermore, the incomplete set of properties given in [1] is not satisfied by the WENO5 weights when the first derivative of the solution vanishes. In particular, at critical points where the third derivative does not simultaneously vanish with the first, WENO5 suffers a loss in accuracy. This formal loss of optimal fifth-order convergence rate has not been previously recognized in the literature. Because solutions will often involve critical points where the first derivative vanishes while the third derivative does not, this behavior is an important issue for many problems.

In this paper, a refinement of the scheme of [1] is developed which has formal fifth-order convergence properties. Using the weights as formulated in [1] as a starting point, the modified scheme renders these weights closer to optimality so as to satisfy sufficient criteria for fifth-order convergence. The resulting scheme maintains its fifth-order accuracy even when ϵ is chosen to be the smallest number possible for a given machine precision. Furthermore, the effects of the parameter ϵ on previous WENO schemes are isolated and examined. Notably, the convergence properties of such schemes are problem-dependent and cannot be known a priori. A detailed derivation of the WENO scheme is given. Section 2 clarifies the concepts of numerical and actual flux, especially as they pertain to the formulation of spatial derivatives in conservation equations. Following the presentation given in [1], the coefficients for the fifth-order upwind scheme, commonly referred to in the literature as the upstream central scheme, are derived. In Section 3, standard concepts behind WENO schemes are elucidated. The candidate stencils for the fifth-order WENO scheme are developed as well as the weights for combining the candidate stencils such that the upstream

central scheme is recovered. Necessary and sufficient conditions on the non-oscillatory weights to achieve fifth-order convergence are derived. Section 4 gives the form of the non-oscillatory weights used in [1]. These weights are shown to violate the necessary conditions for fifth-order convergence near critical points. Furthermore, the order of the scheme is shown to be strongly sensitive to the parameter ϵ. In Section 5, a modification is proposed which formally gives fifth-order convergence at these points. This modification involves mapping the weights as calculated according to [1] to values such that the necessary optimal conditions on the weights are satisfied. As shown for several examples, the new mapped weights retain the ENO behavior. Section 6 addresses the corrections necessary for the WENO schemes up to 11th order.

Several challenging examples of flows with discontinuities are given. In each case, side-by-side comparisons of the predictions of the improved algorithm relative to the original algorithm of [1] show the improvement gives rise to more accurate predictions; however, relative to smooth flows, the accuracy gains are more modest. The achieved convergence rate, determined for the Sod [12] shock tube problem, is roughly first order; a result such as this is not unexpected when any shock capturing scheme is applied to a flow with a discontinuity.

2. Conservation, flux, and numerical flux

A conservative numerical scheme ensures that a quantity remains conserved by calculating a single flux which describes the flow of that quantity between neighboring cells. Though flux conservative schemes are normally formulated using finite volumes, a finite difference scheme is developed here using an approach similar to Shu et al. [6]. In the case that Eq. (1) involves an inhomogeneous source term, these finite difference schemes have the computational advantage of removing the need to integrate such a term over each cell [6].

In order to formulate this finite difference scheme, the discretization shown in Fig. 1 is used. Indices are assigned using the same label for each cell and corresponding node; the position of node j is denoted by x_j, where $j = 0,1,\ldots,N_x$, corresponding to the domain introduced for Eq. (1). Similarly functional values at node j will be denoted by a subscript j (e.g., $f_j = f(x_j)$). Half indices indicate the edges of cells across which fluxes will be calculated. Uniform grid spacing is maintained such that $x_j = x_0 + j\Delta x$, where $\Delta x = \frac{x_{N_x} - x_0}{N_x}$.

Eq. (1) can be approximated by a system of ordinary differential equations, where the spatial derivative has been replaced by a finite difference to yield:

$$\frac{\mathrm{d}u_j}{\mathrm{d}t} = -\frac{f_{j+1/2} - f_{j-1/2}}{\Delta x}. \tag{2}$$

Such a method is conservative since a single flux function is used to describe the flow of a conservative quantity between two cells: $f_{j+1/2}$ describes the flux of u between cells j and $j+1$.

2.1. The numerical flux function

Higher orders of accuracy can be achieved without sacrificing the conservative character of the scheme by considering the form of Eq. (2). Even if f is inconsistent with the actual flux function, u is conserved in an

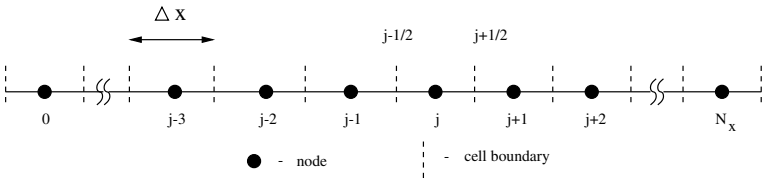

Fig. 1. Computational grid.

infinite domain due to the telescoping cancellation of fluxes between cells. By substituting a different function for f in Eq. (2), the accuracy of this conservative scheme can be increased. Of course any replacement flux function must be chosen such that solutions generated by Eq. (2) approximate in a consistent manner those of the original partial differential equation, Eq. (1).

A function is sought for which the divided difference in Eq. (2) is the exact derivative at x_j rather than only an approximation. Such a function is known in the literature as the numerical flux function, $h(x)$, and satisfies

$$\left.\frac{\partial f}{\partial x}\right|_{x=x_j} = \frac{h_{j+1/2} - h_{j-1/2}}{\Delta x}. \tag{3}$$

Following Shu and Osher [7], $h(x)$ is defined according to

$$f(x) = \frac{1}{\Delta x}\int_{x-\Delta x/2}^{x+\Delta x/2} h(\xi)\,\mathrm{d}\xi. \tag{4}$$

Differentiation of Eq. (4) and evaluation at $x = x_j$ shows that $h(x)$ satisfies Eq. (3) exactly.

Eq. (4) defines $h(x)$ implicitly such that

$$\frac{\mathrm{d}u_j}{\mathrm{d}t} = -\frac{h_{j+1/2} - h_{j-1/2}}{\Delta x} \tag{5}$$

involves no error due to approximating the spatial derivative with a finite difference. Thus $h(x)$ is selected as a replacement for the actual flux in Eq. (2). While $h(x) = f(x) + \mathrm{O}(\Delta x^2)$, as shown in [11], it is clear that $h(x)$ is not the exact flux for a fixed finite Δx.

2.2. Higher order spatial derivatives

By approximating $h(x)$ in Eq. (5), conservative numerical schemes are formulated. These approximations of $h(x)$ are denoted by $\hat{f}(x)$ and are constructed using a polynomial form with undetermined coefficients. Substitution of this polynomial into Eq. (4) leads to a system of equations where the flux is a known quantity at the nodes surrounding the interface of interest, allowing for a unique set of coefficients to be found.

Having found $\hat{f}$, the spatial derivative in Eq. (1) is approximated by

$$\left.\frac{\partial f}{\partial x}\right|_{x=x_j} \approx -\frac{\hat{f}_{j+1/2} - \hat{f}_{j-1/2}}{\Delta x}. \tag{6}$$

Two orders of convergence will be of concern. Clearly the order at which Eq. (6) is satisfied is of primary importance since it is the order at which the overall scheme converges in space. Also the order of individual approximations to the numerical flux, $\hat{f}_{j\pm1/2}$, are important, since they are used to develop the criteria for admissibility of non-oscillatory weights.

2.3. The upstream central scheme

The upstream central scheme is derived by considering a fourth degree polynomial approximation

$$h(x) \approx \hat{f}(x) = a_0 + a_1 x + a_2 x^2 + a_3 x^3 + a_4 x^4, \tag{7}$$

with undetermined coefficients, a_k, where $k = 0, \ldots, 4$. Substituting Eq. (7) into Eq. (4) and performing the integration gives

$$f(x) = a_0 + a_1 x + a_2\left(x^2 + \frac{\Delta x^2}{12}\right) + a_3\left(x^3 + \frac{\Delta x^2 x}{4}\right) + a_4\left(x^4 + \frac{\Delta x^2 x^2}{2}\right). \tag{8}$$

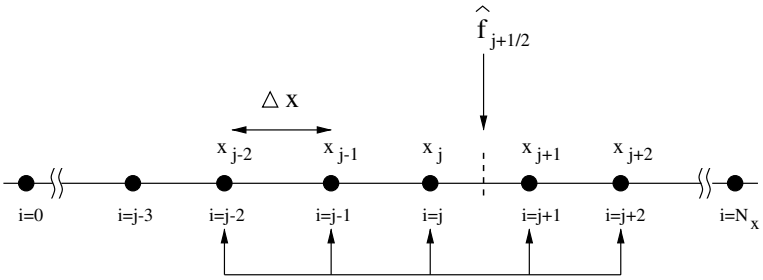

Fig. 2. Upstream central scheme used to compute $\hat{f}_{j+1/2}$.

Referring to Fig. 2, the a_k are found by evaluating Eq. (8) at the stencil nodes, resulting in a system of five equations in the five unknown coefficients. As seen in Fig. 2, the stencil is centered around x_j by using the nodes $x_i = x_j + (i-j)\Delta x$ for $i = j-2, j-1, j, j+1, j+2$. Accordingly, the a_k are found in terms of the nodal fluxes, x_j, and Δx.

Substituting these values for the a_k into Eq. (8) and evaluating the numerical flux at the cell interface $x_{j+1/2}$ gives

$$\begin{aligned}\hat{f}_{j+1/2} &= \tfrac{1}{60}\left(2f_{j-2} - 13f_{j-1} + 47f_j + 27f_{j+1} - 3f_{j+2}\right)\\ &= h_{j+1/2} - \frac{1}{60}\frac{\mathrm{d}^5 f}{\mathrm{d}x^5}\bigg|_{x=x_j}\Delta x^5 + \mathrm{O}(\Delta x^6)\end{aligned} \tag{9}$$

by Taylor series expansion. Note that both x_j and Δx are not present in the leading order term in Eq. (9); thus, it is clear that the resulting stencil is independent of both and may be used to evaluate the numerical flux at any interface in the domain.

To calculate the numerical flux at $x = x_{j-1/2}$, the stencil is shifted to the left by one grid spacing to give

$$\begin{aligned}\hat{f}_{j-1/2} &= \tfrac{1}{60}\left(2f_{j-3} - 13f_{j-2} + 47f_{j-1} + 27f_j - 3f_{j+1}\right)\\ &= h_{j-1/2} - \frac{1}{60}\frac{\mathrm{d}^5 f}{\mathrm{d}x^5}\bigg|_{x=x_j}\Delta x^5 + \mathrm{O}(\Delta x^6)\end{aligned} \tag{10}$$

using another Taylor series expansion. While $\hat{f}_{j\pm1/2}$ only approximates $h_{j\pm1/2}$ to $\mathrm{O}(\Delta x^5)$, the Δx^5 error term is the same for both stencils.

Substitution of Eqs. (9) and (10) into Eq. (6) gives

$$\begin{aligned}\frac{\mathrm{d}f}{\mathrm{d}x}\bigg|_{x_j} &\approx \frac{1}{60}\left(-2f_{j-3} + 15f_{j-2} - 60f_{j-1} + 20f_j + 30f_{j+1} - 3f_{j+2}\right)\\ &= f' + \mathrm{O}(\Delta x^5).\end{aligned} \tag{11}$$

Despite the fact that $\hat{f}$ is only fifth-order accurate and that Eq. (6) involves division by Δx, a fifth-order approximation of the derivative is retained. As a result of using the same stencil to approximate $\hat{f}_{j+1/2}$ and $\hat{f}_{j-1/2}$, the lowest order truncation error terms are equal, as noted, and cancel.

3. Fifth-order WENO schemes

In order for this numerical method to better approximate derivatives near shocks, problems associated with using a large stencil, such as that shown in Fig. 2, must be addressed. In the case of such a large stencil,

a discontinuous solution will affect five different nodes at once and will cause the numerical solution to spuriously oscillate. Thus, a method is sought which smoothly changes the stencil in the neighborhood of a discontinuity in order to avoid these problems. Fifth-order WENO schemes are devised to implement this solution technique [1].

Fifth-order WENO schemes are based on the stencils shown in Fig. 3. A numerical flux, $\hat{f}^k_{j+1/2} = h_{j+1/2} + \mathrm{O}(\Delta x^3)$ with $k \in \{0,1,2\}$, is calculated for each of the three point stencils shown. The $\hat{f}^k_{j+1/2}$ from these stencils are then combined in a weighted average such that in smooth regions this method mimics the central scheme given in Eq. (9). In regions of the flow which contain discontinuities, weights are assigned such that the solution is essentially non-oscillatory.

The numerical flux is now calculated according to

$$h_{j+1/2} \approx \hat{f}_{j+1/2} = \sum_{k=0}^{2} \omega_k \hat{f}^k_{j+1/2}, \tag{12}$$

where ω_k is the weight corresponding to stencil k.

3.1. Formulation of the $\hat{f}^k_{j+1/2}$

Each of the $\hat{f}^k(x)$ calculated gives a third-order approximation of $h(x)$. This is done by the following the same procedure given in Section 2.1. A polynomial form is postulated

$$h(x) \approx \hat{f}^k(x) = b_0 + b_1 x + b_2 x^2, \tag{13}$$

and b_0, b_1 and b_2 are found according to Eq. (4). Thus, for each stencil shown, a different third-order approximation for the numerical flux function is found.

The numerical flux functions for each stencil are found to be

$$\begin{aligned}
\hat{f}^0(x) &= \frac{-f_{j-2} + 2f_{j-1} + 23f_j}{24} + \left(\frac{f_{j-2} - 4f_{j-1} + 3f_j}{2\Delta x}\right)x + \left(\frac{f_{j-2} - 2f_{j-1} + f_j}{2\Delta x^2}\right)x^2,\\
\hat{f}^1(x) &= \frac{-f_{j-1} + 26f_j - f_{j+1}}{24} + \left(\frac{f_{j+1} - f_{j-1}}{2\Delta x}\right)x + \left(\frac{f_{j-1} - 2f_j + f_{j+1}}{2\Delta x^2}\right)x^2,\\
\hat{f}^2(x) &= \frac{23f_j + 2f_{j+1} - f_{j+2}}{24} + \left(\frac{-3f_j + 4f_{j+1} - f_{j+2}}{2\Delta x}\right)x + \left(\frac{f_j - 2f_{j+1} + f_{j+2}}{2\Delta x^2}\right)x^2,
\end{aligned} \tag{14}$$

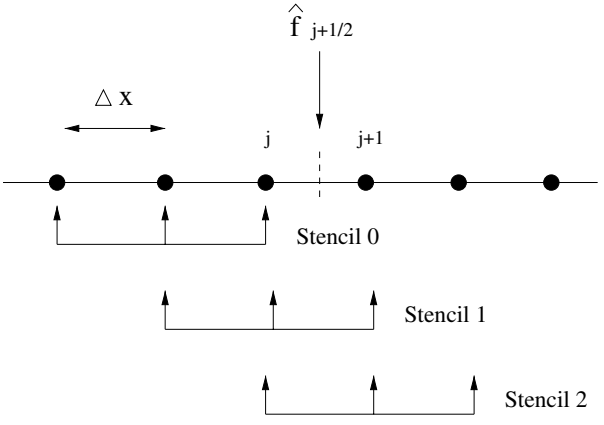

Fig. 3. Stencils used for WENO5 numerical flux.

where the stencils are centered around $x_j = 0$. It is noted that b_1 and $2b_2$ for each equation are finite difference approximations of f'_j or f''_j, respectively.

These approximations are evaluated at the $j + 1/2$ interface to give the $\hat{f}^k_{j+1/2}$ of Eq. (12):

$$\begin{aligned}
\hat{f}^0_{j+1/2} &= \tfrac{1}{6}(2f_{j-2} - 7f_{j-1} + 11f_j),\\
\hat{f}^1_{j+1/2} &= \tfrac{1}{6}(-f_{j-1} + 5f_j + 2f_{j+1}),\\
\hat{f}^2_{j+1/2} &= \tfrac{1}{6}(2f_j + 5f_{j+1} - f_{j+2}).
\end{aligned} \tag{15}$$

Since these linear combinations define the numerical flux at every cell boundary in the domain, one needs only to shift each index by -1 to arrive at the corresponding $\hat{f}^k_{j-1/2}$.

The Taylor series expansions of Eq. (15) give

$$\begin{aligned}
\hat{f}^0_{j\pm1/2} &= h_{j\pm1/2} - \tfrac{1}{4}f'''(0)\Delta x^3 + \mathrm{O}(\Delta x^4),\\
\hat{f}^1_{j\pm1/2} &= h_{j\pm1/2} + \tfrac{1}{12}f'''(0)\Delta x^3 + \mathrm{O}(\Delta x^4),\\
\hat{f}^2_{j\pm1/2} &= h_{j\pm1/2} - \tfrac{1}{12}f'''(0)\Delta x^3 + \mathrm{O}(\Delta x^4).
\end{aligned} \tag{16}$$

Note that each of these takes the form

$$\hat{f}^k_{j\pm1/2} = h_{j\pm1/2} + A_k\Delta x^3 + \mathrm{O}(\Delta x^4), \quad k \in \{0,1,2\}. \tag{17}$$

Here the third-order error term has been explicitly written in Eq. (16) since it will become important in deriving constraints on the non-oscillatory weights.

Note also from Eq. (16) that

$$\frac{1}{\Delta x}\left(\hat{f}^n_{j+1/2} - \hat{f}^m_{j-1/2}\right) = \begin{cases} \frac{\partial f}{\partial x}\big|_{x=x_j} + \mathrm{O}(\Delta x^2) & \text{if } n \neq m,\\ \frac{\partial f}{\partial x}\big|_{x=x_j} + \mathrm{O}(\Delta x^3) & \text{if } n = m. \end{cases} \tag{18}$$

3.2. Ideal weights

In regions of smooth flow, the linear combination of the $\hat{f}^k_{j+1/2}$ given in Eq. (12) should reduce to the central scheme, since the central scheme gives the optimal convergence properties possible for a five point stencil (cf. Figs. 2 and 3). These weights are thus known in the literature as the ideal weights. Substituting Eq. (15) into Eq. (12) gives the numerical flux for fifth-order WENO schemes. Setting this numerical flux equal to the upstream central scheme given in Eq. (9) gives

$$\begin{aligned}
\hat{f}_{j+1/2} &= \frac{1}{6}\begin{pmatrix} 2f_{j-2} - 7f_{j-1} + 11f_j\\ -f_{j-1} + 5f_j + 2f_{j+1}\\ 2f_j + 5f_{j+1} - f_{j+2}\end{pmatrix}^{\mathrm{T}} \cdot \begin{pmatrix}\bar{\omega}_0\\ \bar{\omega}_1\\ \bar{\omega}_2\end{pmatrix}\\
&= \frac{1}{60}\left(2f_{j-2} - 13f_{j-1} + 47f_j + 27f_{j+1} - 3f_{j+2}\right),
\end{aligned} \tag{19}$$

where $\bar{\omega}_i$ is the ith ideal weight. These weights, which satisfy

$$\sum_{k=0}^{2}\bar{\omega}_k\hat{f}^k_{j+1/2} = h_{j+1/2} + \mathrm{O}(\Delta x^5) \tag{20}$$

are given by

$$\bar{\omega}_0 = 1/10, \quad \bar{\omega}_1 = 6/10 \quad \text{and} \quad \bar{\omega}_2 = 3/10. \tag{21}$$

Note that they sum to unity. Furthermore, use of this stencil results in $f'(x) = \frac{h_{j+1/2} - h_{j-1/2}}{\Delta x} + \mathrm{O}(\Delta x^5)$, as seen in Section 2.2.

3.3. Non-oscillatory weights

In order to achieve the optimal order approximation to $h_{j+1/2}$ in smooth regions, the weights must converge in an appropriate manner to the ideal weights as Δx approaches zero; however, in regions where a discontinuity does exist, the weights should effectively remove the contribution of stencils which contain the discontinuity.

In order to arrive at appropriate criteria for the weights, consider that the numerical flux function is given by

$$\hat{f}_{j\pm1/2} = \sum_{k=0}^{2} \omega_k \hat{f}^k_{j\pm1/2}, \tag{22}$$

where $\hat{f}^k_{j\pm1/2} = h_{j\pm1/2} + A_k \Delta x^3 + \mathrm{O}(\Delta x^4)$. Adding and subtracting $\sum_{k=0}^{2} \bar{\omega}_k \hat{f}^k_{j\pm1/2}$ from Eq. (22) and comparing with Eq. (20) gives

$$\hat{f}_{j\pm1/2} = \underbrace{\sum_{k=0}^{2} \bar{\omega}_k \hat{f}^k_{j\pm1/2}}_{h_{j\pm1/2} + \mathrm{O}(\Delta x^5)} + \sum_{k=0}^{2} (\omega_k - \bar{\omega}_k) \hat{f}^k_{j\pm1/2}, \tag{23}$$

where the second term must be at least an $\mathrm{O}(\Delta x^6)$ quantity in order for the derivative to be approximated at fifth order.

Expanding this second term gives

$$\begin{aligned} \sum_{k=0}^{2} (\omega_k - \bar{\omega}_k) \hat{f}^k_{j\pm1/2} &= \sum_{k=0}^{2} (\omega_k - \bar{\omega}_k)(h_{j\pm1/2} + A_k \Delta x^3 + \mathrm{O}(\Delta x^4)) \\ &= h_{j\pm1/2} \sum_{k=0}^{2} (\omega_k - \bar{\omega}_k) + \Delta x^3 \sum_{k=0}^{2} A_k (\omega_k - \bar{\omega}_k) + \sum_{k=0}^{2} (\omega_k - \bar{\omega}_k) \mathrm{O}(\Delta x^4). \end{aligned} \tag{24}$$

Thus, it is sufficient to require

$$\sum_{k=0}^{2} (\omega_k - \bar{\omega}_k) = \mathrm{O}(\Delta x^6) \tag{25a}$$

and

$$\omega_k - \bar{\omega}_k = \mathrm{O}(\Delta x^3) \tag{25b}$$

for the overall scheme to retain fifth-order accuracy. Note that, while these conditions are not necessary, they serve as a simple set of criteria around which to design the non-oscillatory weights.

Thus far, the accuracy requirements have been found by considering each individual numerical flux in isolation; however, Eq. (6) reveals that it is the difference in the numerical fluxes across a cell which actually determines the accuracy of the scheme. In considering $\hat{f}_{j+1/2} - \hat{f}_{j-1/2} = f'(x)\Delta x + \mathrm{O}(\Delta x^6)$, it will be shown that Eq. (25b) may be relaxed.

Employing the same technique using in deriving Eq. (23), comparison of the ideal weights with the non-oscillatory weights conveniently identifies the error terms. In this case, however, the constraints are found by examination of the the error terms which result from subtraction of the numerical fluxes:

$$\hat{f}_{j+1/2}-\hat{f}_{j-1/2}=\overbrace{\sum_{k=0}^{2}\bar{\omega}_k\hat{f}^k_{j+1/2}-\sum_{k=0}^{2}\bar{\omega}_k\hat{f}^k_{j-1/2}}^{f'_j+\mathrm{O}(\Delta x^6)}+\sum_{k=0}^{2}(\omega_k^{(+)}-\bar{\omega}_k)\hat{f}^k_{j+1/2}-\sum_{k=0}^{2}(\omega_k^{(-)}-\bar{\omega}_k)\hat{f}^k_{j-1/2}, \tag{26}$$

where superscript (+) or (−) on ω_k indicate their use in either $\hat{f}_{j+1/2}$ or $\hat{f}_{j-1/2}$ stencil. Expanding the last two terms in Eq. (26) and substituting for $\hat{f}^k_{j\pm1/2}$ from Eq. (16), the criteria for fifth-order convergence are found to be

$$\sum_{k=0}^{2}(\omega_k^{(\pm)}-\bar{\omega}_k)=\mathrm{O}(\Delta x^6), \tag{27a}$$

$$\sum_{k=0}^{2}A_k(\omega_k^{(+)}-\omega_k^{(-)})=\mathrm{O}(\Delta x^3) \tag{27b}$$

and

$$\omega_k^{(\pm)}-\bar{\omega}_k=\mathrm{O}(\Delta x^2). \tag{27c}$$

Carrying out the sum in Eq. (27b) yields

$$-\frac{1}{12}\left(3\omega_1^{(+)}-3\omega_1^{(-)}-\omega_2^{(+)}+\omega_2^{(-)}+\omega_3^{(+)}-\omega_3^{(-)}\right)f'''(0)=\mathrm{O}(\Delta x^3) \tag{28}$$

taking into account that the A_k are given explicitly in Eq. (16).

Thus to retain fifth-order accuracy, the necessary and sufficient conditions are

$$\sum_{k=0}^{2}(\omega_k-\bar{\omega}_k)=\mathrm{O}(\Delta x^6), \tag{29a}$$

$$(3\omega_1^{(+)}-3\omega_1^{(-)}-\omega_2^{(+)}+\omega_2^{(-)}+\omega_3^{(+)}-\omega_3^{(-)})=\mathrm{O}(\Delta x^3) \tag{29b}$$

and

$$(\omega_k-\bar{\omega}_k)=\mathrm{O}(\Delta x^2). \tag{29c}$$

Here Eqs. (29a) and (29c) constrain both the "+" and "−" stencil, and thus the superscript (±) has been dropped.

Note that the non-oscillatory weights developed in [1] are formulated by appealing to Eqs. (29a) and (29c) only (cf. $\sum_{k=0}^{2}\omega_k=1$ and Eq. (2.14) with $r=3$ in [1, p. 205]). Eq. (29b) is not presented there and thus the constraints presented in [1] are incomplete. Comparison of Eqs. (25) and (29) reveals that the relaxation of Eq. (25b) by one order of accuracy requires that Eq. (29b) be satisfied as well. Unfortunately, Eq. (29b) is a difficult constraint to use in the design of the non-oscillatory weights.

4. The non-oscillatory weights of [1]

The development of fifth-order WENO schemes up to this point has been general, culminating in Eqs. (25) and (29). All WENO schemes employing the candidate stencils in Fig. 3 retaining fifth-order convergence properties must satisfy Eq. (29). The weights as designed in [1] are the focus of this section. This scheme is denoted WENO5 in order to conform with the literature to date.

4.1. Formulation of $\omega_k^{(JS)}$

In an attempt to satisfy these constraints, weights were formulated in [1] according to

$$\omega_k^{(\mathrm{JS})} = \frac{\alpha_k}{\sum_{i=0}^{2}\alpha_i}, \quad \text{where } \alpha_k = \frac{\bar{\omega}_k}{(\epsilon+\beta_k)^p}, \tag{30}$$

and a superscript (JS) is given to ω_k to denote the non-oscillatory weights as developed by Jiang and Shu [1]. Here, ϵ is a small parameter chosen such that α_k remains bounded, β_k is the indicator of smoothness for the $\hat{f}^k_{j+1/2}$ approximation of the numerical flux, and p is chosen in order to allow for weights in non-smooth regions to approach zero at an accelerated rate as $\Delta x \to 0$. In much of the literature, the indicator of smoothness is denoted by IS. It is easy to see that Eq. (29a) is satisfied since $\sum_{k=0}^{2}\omega_k^{(\mathrm{JS})} = \sum_{k=0}^{2}\bar{\omega}_k = 1$ by construction.

The indicators of smoothness as incorporated in Eq. (30) will provide a measure of the smoothness of a solution over a particular stencil. Furthermore, the β_k's must be chosen such that each $\omega_k^{(\mathrm{JS})}$ approaches the ideal weight at a fast enough convergence rate, according to Eq. (29c). For the present analysis, ϵ is assumed to be 0. The role of ϵ will be analyzed in Section 4.3.

It is assumed that the indicator of smoothness can be written as

$$\beta_k = D(1+\mathrm{O}(\Delta x)^2), \tag{31}$$

where D is some non-zero constant independent of k. Substitution of Eq. (31) into Eq. (30) gives

$$\alpha_k = \frac{\bar{\omega}_k}{(D(1+\mathrm{O}(\Delta x)^2))^p} = \frac{\bar{\omega}_k}{D^p}(1+\mathrm{O}(\Delta x^2)). \tag{32}$$

The sum of these terms is given by

$$\sum_{k=0}^{2}\alpha_k = \frac{1}{D^p}(1+\mathrm{O}(\Delta x^2)) \tag{33}$$

taking into account that $\sum_{k=0}^{2}\bar{\omega}_k = 1$. Thus $\omega_k^{(\mathrm{JS})}$, as defined in Eq. (30), is given by

$$\omega_k^{(\mathrm{JS})} = \bar{\omega}_k + \mathrm{O}(\Delta x^2), \tag{34}$$

which agrees with Eq. (29c). Note that Eq. (29b) is still not satisfied by enforcing Eq. (31).

4.2. Indicators of smoothness

It remains to find a set of β_k which satisfy Eq. (31). Following [1], the indicators of smoothness are defined by

$$\beta_k = \sum_{i=1}^{2}\Delta x^{2i-1}\int_{x_{j-1/2}}^{x_{j+1/2}}\left(\frac{\mathrm{d}^i\hat{f}^k}{\mathrm{d}x^i}\right)^2 \mathrm{d}x. \tag{35}$$

Since $\hat{f}^k = b_0 + b_1 x + b_2 x^2$, this equation simplifies to

$$\beta_k = b_1^2\Delta x^2 + \frac{13 b_2^2 \Delta x^4}{3}, \tag{36}$$

where the stencils are centered around $x_j = 0$. Substituting b_1 and b_2 from Eq. (14), the indicators of smoothness take on a particularly intuitive form:

$$\begin{aligned}
\beta_0 &= \frac{13}{12}\Big(\underbrace{f_{j-2}-2f_{j-1}+f_j}_{\Delta x^2(f_j''+\mathrm{O}(\Delta x))}\Big)^2+\frac{1}{4}\Big(\underbrace{f_{j-2}-4f_{j-1}+3f_j}_{2\Delta x(f_j'+\mathrm{O}(\Delta x^2))}\Big)^2,\\
\beta_1 &= \frac{13}{12}\Big(\underbrace{f_{j-1}-2f_j+f_{j+1}}_{\Delta x^2(f_j''+\mathrm{O}(\Delta x^2))}\Big)^2+\frac{1}{4}\Big(\underbrace{f_{j+1}-f_{j-1}}_{2\Delta x f_j'+\mathrm{O}(\Delta x^2)}\Big)^2,\\
\beta_2 &= \frac{13}{12}\Big(\underbrace{f_j-2f_{j+1}+f_{j+2}}_{\Delta x^2(f_j''+\mathrm{O}(\Delta x))}\Big)^2+\frac{1}{4}\Big(\underbrace{3f_j-4f_{j+1}+f_{j+2}}_{-2\Delta x(f_j'+\mathrm{O}(\Delta x^2))}\Big)^2.
\end{aligned} \tag{37}$$

Expansion of Eq. (37) in Taylor series about f_j gives

$$\begin{aligned}
\beta_0 &= f'^2\Delta x^2+\left(\frac{13}{12}f''^2-\frac{2}{3}f'f'''\right)\Delta x^4+\left(-\frac{13}{6}f''f'''+\frac{1}{2}f'f^{(4)}\right)\Delta x^5+\mathrm{O}(\Delta x^6),\\
\beta_1 &= f'^2\Delta x^2+\left(\frac{13}{12}f''^2+\frac{1}{3}f'f'''\right)\Delta x^4+\mathrm{O}(\Delta x^6),\\
\beta_2 &= f'^2\Delta x^2+\left(\frac{13}{12}f''^2-\frac{2}{3}f'f'''\right)\Delta x^4+\left(\frac{13}{6}f''f'''-\frac{1}{2}f'f^{(4)}\right)\Delta x^5+\mathrm{O}(\Delta x^6).
\end{aligned} \tag{38}$$

Referring to Table 1, the β_k are of the form Eq. (31) for $f' \neq 0$.

However, for the case that $f' = \mathrm{O}(\Delta x)$, the indicators of smoothness, β_0 and β_2, do not satisfy the constraint given in Eq. (31). Thus, $\omega_k^{(\mathrm{JS})}$ does not approach $\bar{\omega}_k$ at a fast enough rate of convergence to achieve fifth-order accuracy near critical points. Rather,

$$\omega_k^{(\mathrm{JS})} = \bar{\omega}_k + \mathrm{O}(\Delta x) \tag{39}$$

near critical points. One should note the discrepancy between the β_0 and β_2 in Table 1 and those reported in [1, Eqs. (3.5), (3.7) and (3.9)].

To demonstrate this discrepancy, one must consider an example in which $f' = 0$ at a point for which $f''' \neq 0$. Note that the example functions used in [1], namely $\sin(x)$ and $\sin^4(x)$, do not satisfy this criterion since they give $f' = f''' = 0$ at critical points. Due to this fact, as well as the introduction of ϵ into the weights, the convergence test of [1] is unable to detect this potential loss of accuracy at critical points.

4.3. The role of ϵ

In order to understand the convergence behavior of WENO5 in much of the literature, a better understanding of the parameter ϵ in Eq. (30) is required.

It should first be noticed that ϵ appears as a dimensional quantity in Eq. (30) [11]. Thus ϵ is normally selected on a case by case basis, which belies the fact that ϵ changes the order of convergence and is not simply selected so as to prevent an indeterminate form in Eq. (30).

Table 1
Orders of β_k written for comparison with Eq. (31)

$f' \neq 0$	$f' = 0$
$\beta_0 = (f'\Delta x)^2(1+\mathrm{O}(\Delta x^2))$	$\beta_0 = \frac{13}{12}(f''\Delta x^2)^2(1+\mathrm{O}(\Delta x))$
$\beta_1 = (f'\Delta x)^2(1+\mathrm{O}(\Delta x^2))$	$\beta_1 = \frac{13}{12}(f''\Delta x^2)^2(1+\mathrm{O}(\Delta x^2))$
$\beta_2 = (f'\Delta x)^2(1+\mathrm{O}(\Delta x^2))$	$\beta_2 = \frac{13}{12}(f''\Delta x^2)^2(1+\mathrm{O}(\Delta x))$

Substitution of Eq. (38) into Eq. (30) leads to

$$\omega_k^{(\mathrm{JS})} = \frac{\alpha_k}{\sum_{i=0}^{2}\alpha_i}, \tag{40a}$$

where

$$\alpha_k = \frac{\bar{\omega}_k}{\epsilon + f'^2\Delta x^2 + \mathrm{O}(\Delta x^4)}. \tag{40b}$$

As $\Delta x \to 0$ in smooth regions of flow, the denominator of Eq. (40b) is eventually dominated by ϵ, and the indicators of smoothness become inconsequential. Of course, the magnitude of ϵ determines at what resolution ϵ becomes the dominant term. As ϵ begins to dominate, the predictions of the WENO5 scheme approach those of the central difference scheme, as is verified by considering Eq. (30) with $\beta_k = 0$. Furthermore, oscillations of order ϵ^2 can exist near discontinuities, so choosing an ϵ which is too large mitigates the ENO behavior of the method.

The choice of ϵ should also depend on the particular machine performing the calculations. To avoid division by zero, ϵ can be slightly larger than the square root of the smallest positive number allowed for a particular machine. According to the IEEE standard [13], this roughly translates to $\epsilon > 10^{-18}$ for 32-bit floating point arithmetic (single precision), $\epsilon > 10^{-153}$ for 64-bit floating point arithmetic (double precision) and $\epsilon > 10^{-2467}$ for 128-bit floating point arithmetic (quadruple precision). For schemes beyond 11th order, i.e., schemes with potentially very small numerators in Eq. (30), these weights may need to be increased slightly to avoid computing outside the range of machine precision. In the following Sections 4.5, 5.1 and 5.3, 128-bit floating point arithmetic was utilized to ensure machine precision is not playing a role. In Sections 5.4 and 5.5, only 64-bit floating point arithmetic was used, since the solutions involving captured shocks are not so accurate as to necessitate the higher precision.

4.4. The WENO5 scheme

The final form of the WENO5 scheme as published in [1] is thus given by

$$\left.\frac{\mathrm{d}f}{\mathrm{d}x}\right|_{x_j} = \frac{\hat{f}_{j+1/2} - \hat{f}_{j-1/2}}{\Delta x} \tag{41a}$$

and

$$\hat{f}_{j\pm1/2} = \sum_{k=0}^{2} \omega_k^{(\mathrm{JS})} \hat{f}^k_{j\pm1/2}, \tag{41b}$$

where the weights in Eq. (12) are explicitly denoted as those developed in [1]. These weights are given in Eq. (30), and the β_k are given in Eq. (37).

4.5. A simple example

Measuring the convergence of the WENO5 method to $f'(0) = 0$ for

$$f(x) = x^3 + \cos(x), \tag{42}$$

will demonstrate the expected loss in accuracy, since $f'(0) = 0$ and $f'''(0) = 6$. Also, the effect ϵ has on the achieved rate of convergence is illustrated and explained. The function and its first and third derivatives are shown in Fig. 4.

Examining the indicators of smoothness while resolving Δx clarifies how a fixed ϵ eventually becomes the dominant factor in determining the non-oscillatory weights. In Table 2, Δx is resolved from 10^{-3} to

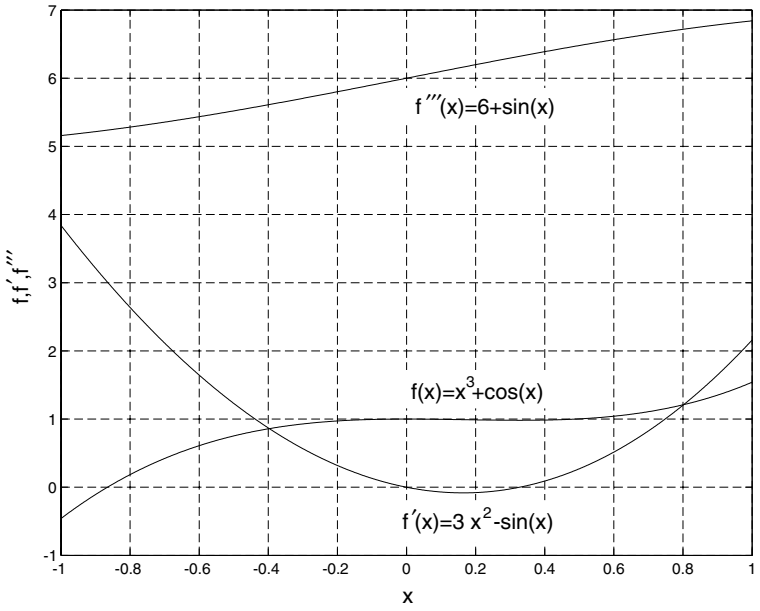

Fig. 4. Flux function from Section 4.5. Also shown are the first and third spatial derivatives. Note there are two critical points, both of which have a non-vanishing third spatial derivative.

Table 2
Indicators of smoothness for calculation of $\frac{df}{dx}\big|_{x=0}$, where $f(x) = x^3 + \cos(x)$

Δx	β_0	β_1	β_2
1.00×10^{-3}	1.09638×10^{-12}	1.08333×10^{-12}	1.07038×10^{-12}
	2.11149×10^{-12}	2.10439×10^{-12}	2.08533×10^{-12}
5.00×10^{-4}	6.81152×10^{-14}	6.77083×10^{-14}	6.73027×10^{-14}
	1.31086×10^{-13}	1.30865×10^{-13}	1.30271×10^{-13}
2.50×10^{-4}	4.24448×10^{-15}	4.23177×10^{-15}	4.21909×10^{-15}
	8.16540×10^{-15}	8.15854×10^{-15}	8.13997×10^{-15}
1.25×10^{-4}	2.64883×10^{-16}	2.64486×10^{-16}	2.64089×10^{-16}
	5.09481×10^{-16}	5.09267×10^{-16}	5.08687×10^{-16}
6.25×10^{-5}	1.65428×10^{-17}	1.65304×10^{-17}	1.65180×10^{-17}
	3.18159×10^{-17}	3.18092×10^{-17}	3.17911×10^{-17}

For each successive value of Δx, the first row of indicators shown are used in calculating $\hat{f}_{+1/2}$ while the second are used for calculating $\hat{f}_{-1/2}$.

6.25×10^{-5} by factors of two. The indicators of smoothness approach zero at the rates given in Table 1 and range from approximately 10^{-12} to approximately 10^{-17} as the grid is resolved. Thus for $\epsilon \in [10^{-12}, 10^{-17}]$, ϵ will change the order of convergence of the scheme as the grid is resolved, since it will begin to dominate the β_k at some point in the grid convergence process.

To demonstrate this behavior, results are compared for $\epsilon \in \{10^{-40}, 10^{-15}, 10^{-6}\}$ with one another and with the results from the central scheme. Table 3 shows the error in approximating $\partial f/\partial x$ for $f(x) = x^3 + \cos(x)$ at $x = 0$. Also shown are the rates of convergence, r_c, of each scheme. For $\epsilon = 10^{-40}$, the WENO5 scheme is confirmed to be third-order accurate at the critical point. As the size of ϵ is increased

Table 3
Convergence properties of WENO5 as implemented in [1] near a critical point

WENO5 as implemented in [1]				Upstream central scheme		
ϵ	Δx	r_c	Error	Δx	r_c	Error
10^{-40}	1.00×10^{-3}	–	1.63079×10^{-9}	1.00×10^{-3}	–	1.66667×10^{-17}
	5.00×10^{-4}	2.95774	2.09907×10^{-10}	5.00×10^{-4}	5.00000	5.20833×10^{-19}
	2.50×10^{-4}	2.97924	2.66187×10^{-11}	2.50×10^{-4}	5.00000	1.62760×10^{-20}
	1.25×10^{-4}	2.98971	3.35115×10^{-12}	1.25×10^{-4}	5.00000	5.08626×10^{-22}
	6.25×10^{-5}	2.99488	4.20384×10^{-13}	6.25×10^{-5}	5.00000	1.58946×10^{-23}
10^{-15}	1.00×10^{-3}	–	1.63016×10^{-9}			
	5.00×10^{-4}	2.96716	2.08462×10^{-10}			
	2.50×10^{-4}	3.13003	2.38119×10^{-11}			
	1.25×10^{-4}	4.38773	1.13751×10^{-12}			
	6.25×10^{-5}	6.45124	1.29998×10^{-14}			
10^{-6}	1.00×10^{-3}	–	3.62634×10^{-15}			
	5.00×10^{-4}	6.98214	2.86836×10^{-17}			
	2.50×10^{-4}	6.92438	2.36150×10^{-19}			
	1.25×10^{-4}	6.72923	2.22582×10^{-21}			
	6.25×10^{-5}	6.24690	2.93079×10^{-23}			

to 10^{-15}, this parameter begins to dominate the indicator of smoothness. The use of $\epsilon = 10^{-6}$ is shown, since it is recommended in the literature [1]. For this case, the method is ostensibly even seventh-order convergent at the first level of resolution, dropping to lower orders as the method becomes almost equivalent to the central scheme.

It is clear that the order of the WENO5 scheme is dependent on the size of ϵ and the level of grid resolution. Thus it becomes difficult, if not impossible, to determine the order of the WENO5 scheme for a complicated problem a priori at a given grid resolution.

One may inquire into the behavior of fifth-order WENO schemes at critical points of higher order (i.e., f' and f'' are zero). To answer this, consider that the indicators of smoothness, as given by Eqs. (36) and (14), are linear combinations of derivatives evaluated at the stencil midpoint. In the case where the component stencils are third-order polynomials, only the first and and second derivatives can be approximated. When both of these are zero at the midpoint of the stencil, the indicator of smoothness will no longer approximate a non-zero quantity. In other words, the indicators of smoothness are determined to the lowest order by truncation error. Thus Eq. (31) is not satisfied, since such an error will, in general, not admit a single lowest order term, D, for all the β_k. This results in a loss of accuracy.

5. Fifth-order mapped WENO (WENO5M)

Formulation of the weights as introduced in [1] is both intuitive and fifth-order accurate for smooth flows except near critical points. Thus, rather than attempt to formulate a new indicator of smoothness which allows our weights to satisfy Eq. (29), the $\omega_k^{(JS)}$ are used as a first approximation and mapped to more accurate values so that Eq. (25) is satisfied.

5.1. The correction

To increase the accuracy of these weights, consider the functions

$$g_k(\omega) = \frac{\omega(\bar{\omega}_k + \bar{\omega}_k^2 - 3\bar{\omega}_k\omega + \omega^2)}{\bar{\omega}_k^2 + \omega(1 - 2\bar{\omega}_k)}, \qquad \bar{\omega}_k \in (0,1) \tag{43}$$

for $k = 0, 1, 2$. All of these functions have the following features: they are monotonically increasing with finite slope, $g_k(0) = 0,\ g_k(1) = 1,\ g_k(\bar{\omega}_k) = \bar{\omega}_k,\ g_k'(\bar{\omega}_k) = 0$ and $g_k''(\bar{\omega}_k) = 0$. These functions are shown in Fig. 5.

A more accurate approximation of the weights is given by

$$\alpha_k^* = g_k(\omega_k^{(\mathrm{JS})}). \tag{44}$$

To understand this process, it is instructive to view each $g_k(\omega)$ as a mapping. For each k, $g_k(\omega)$ becomes flat in the neighborhood of the kth ideal weight. Thus $\omega_k^{(\mathrm{JS})}$, which is in an $\mathrm{O}(\Delta x)$ neighborhood of $\bar{\omega}_k$ according to Eq. (39), can be used as an initial guess which is mapped to a more accurate value by $g_k(\omega)$. For values of $\omega_k^{(\mathrm{JS})}$ which are close to 0 or 1, the mapping has a minimal effect. This behavior can be seen geometrically from inspection of Fig. 5 and consideration of the identity mapping.

Evaluation at $\omega_k^{(\mathrm{JS})}$ of the Taylor series approximations of the $g_k(\omega)$ about $\bar{\omega}_k$ yield

$$\begin{aligned}\alpha_k^* &= g_k(\bar{\omega}_k) + g_k'(\bar{\omega}_k)\left(\omega_k^{(\mathrm{JS})} - \bar{\omega}_k\right) + \frac{g_k''(\bar{\omega}_k)}{2}\left(\omega_k^{(\mathrm{JS})} - \bar{\omega}_k\right)^2 + \frac{g_k'''(\bar{\omega}_k)}{6}\left(\omega_k^{(\mathrm{JS})} - \bar{\omega}_k\right)^3 + \cdots \\ &= \bar{\omega}_k + \frac{\left(\omega_k^{(\mathrm{JS})} - \bar{\omega}_k\right)^3}{\bar{\omega}_k - \bar{\omega}_k^3} + \cdots \\ &= \bar{\omega}_k + \mathrm{O}(\Delta x^3).\end{aligned} \tag{45}$$

The modified weights are defined according to

$$\omega_k^{(\mathrm{M})} = \frac{\alpha_k^*}{\sum_{i=0}^{2}\alpha_i^*} \quad \text{where } \frac{1}{\sum_{i=0}^{2}\alpha_i^*} = 1 + \mathrm{O}(\Delta x^3), \tag{46}$$

again taking into account that $\sum_{k=0}^{2}\bar{\omega}_k = 1$. Here a superscript (M) has been added to signify the weights use in WENO5M. Thus,

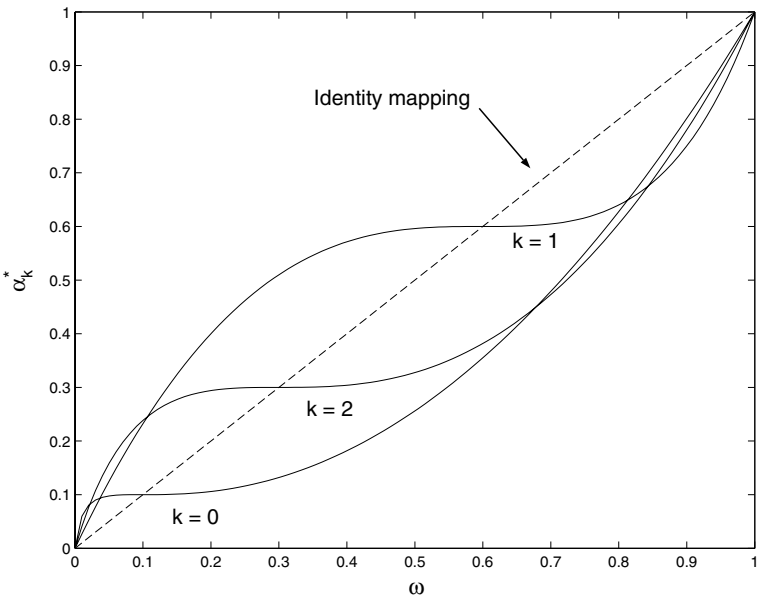

Fig. 5. Mapping functions used with the modified WENO5 scheme given in Section 5. Notice the identity mapping, also shown, identifies the stationary points for the α_k^* maps. Each α_k^* becomes flat in the region around the corresponding $\bar{\omega}_k$, which effectively maps an $\omega^{(\mathrm{JS})}$ in this region to a more accurate approximation of the ideal weight.

$$\sum_{k=0}^{2} \omega_k^{(\mathrm{M})} = 1 \quad \text{and} \quad \omega_k^{(\mathrm{M})} = \bar{\omega}_k + \mathrm{O}(\Delta x^3) \tag{47}$$

which satisfies Eq. (25). Thus the method is fifth-order accurate even near critical points where $f' = 0$. Note that implementation of this correction requires only a slight alteration to the existing WENO5 interpolation scheme.

For comparison, the results using the mapped fifth-order WENO (WENO5M) scheme on the example problem given in Section 4.5 are given in Table 4. The method is shown to be fifth-order accurate with $\epsilon = 10^{-40}$.

5.2. The WENO5M scheme

The final form of the WENO5M scheme is thus given by

$$\left.\frac{\mathrm{d}f}{\mathrm{d}x}\right|_{x_j} = \frac{\hat{f}_{j+1/2} - \hat{f}_{j-1/2}}{\Delta x} \tag{48a}$$

and

$$\hat{f}_{j\pm1/2} = \sum_{k=0}^{2} \omega_k^{(\mathrm{M})} \hat{f}^k_{j\pm1/2}, \tag{48b}$$

where the weights in Eq. (12) are explicitly denoted as the mapped weights. These weights are given in Eq. (46) where $\alpha_k^* = g_k(\omega_k^{(\mathrm{JS})})$. Here, $\omega_k^{(\mathrm{JS})}$ is given in Eqs. (30) and (37).

5.3. Linear advection example

As an example, consider

$$\frac{\partial u}{\partial t} + \frac{\partial u}{\partial x} = 0 \quad \text{on } x \in [-1, 1], \;\; t \in [0, 2] \tag{49}$$

with the initial condition

$$u(x, t = 0) = \sin\left(\pi x - \frac{\sin(\pi x)}{\pi}\right) \tag{50}$$

and periodic boundary conditions, $u|_{x=-1} = u|_{x=1}$. Here $x_0 = -1$, $x_N = 1$, and the flux f is simply the conserved quantity itself, u. This particular initial condition has two critical points at which $f' = 0$ and $f''' \neq 0$ as seen in Fig. 6.

Table 4
Convergence properties of WENO5M

WENO5M scheme ($\epsilon = 10^{-40}$)			Upstream central scheme		
Δx	r_c	Error	Δx	r_c	Error
1.00×10^{-3}	–	6.14598×10^{-14}	1.00×10^{-3}	–	1.66667×10^{-17}
5.00×10^{-4}	4.86269	2.11240×10^{-15}	5.00×10^{-4}	5.00000	5.20833×10^{-19}
2.50×10^{-4}	4.93600	6.90069×10^{-17}	2.50×10^{-4}	5.00000	1.62760×10^{-20}
1.25×10^{-4}	4.96904	2.20324×10^{-18}	1.25×10^{-4}	5.00000	5.08626×10^{-22}
6.25×10^{-5}	4.98477	6.95818×10^{-20}	6.25×10^{-5}	5.00000	1.58946×10^{-23}

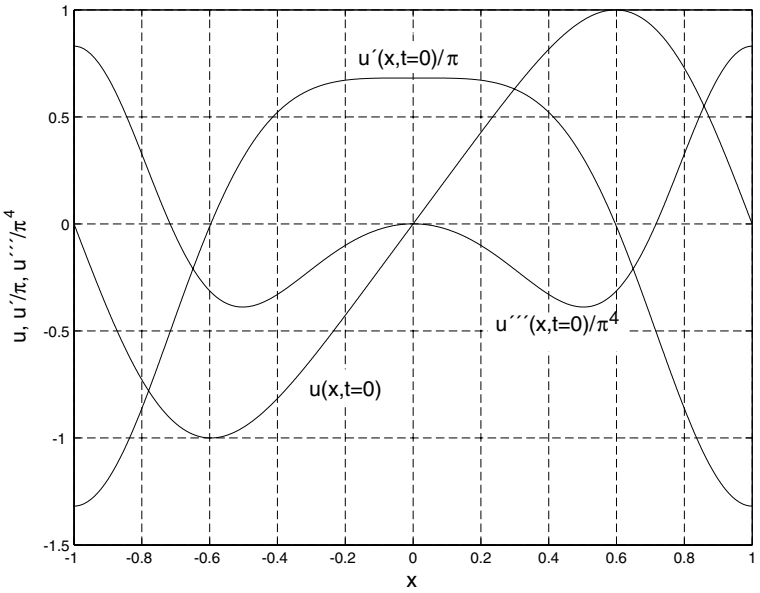

Fig. 6. The initial condition, $u(x,t=0)=\sin(\pi x-\frac{\sin(\pi x)}{\pi})$, used for the example problem given in Section 5.3. Also shown are the first and third derivatives. Note that there are two critical points which all have a non-vanishing third derivative.

The exact solution to Eqs. (49) and (50) is easily found using the method of characteristics and is given by

$$u_{\text{exact}}(x,t)=\sin\left(\pi(x-t)-\frac{\sin(\pi(x-t))}{\pi}\right). \tag{51}$$

Spatial discretization of $\partial u/\partial x$ in Eq. (49) is done using the upstream central scheme, the WENO5M scheme with $\epsilon=10^{-40}$, and the WENO5 scheme with $\epsilon=10^{-6}$ and 10^{-40}. For each case, the resulting set of ordinary differential equations in time are solved discretely using a third-order Runge–Kutta method given by

$$\begin{aligned} u^{*} &= u^{n}+\Delta t\mathscr{L}(u^{n}),\\ u^{**} &= \tfrac{3}{4}u^{n}+\tfrac{1}{4}u^{*}+\tfrac{1}{4}\Delta t\mathscr{L}(u^{*}),\\ u^{n+1} &= \tfrac{1}{3}u^{n}+\tfrac{2}{3}u^{**}+\tfrac{2}{3}\Delta t\mathscr{L}(u^{**}), \end{aligned} \tag{52}$$

where $\mathscr{L}=-\frac{\hat{f}_{j+1/2}-\hat{f}_{j-1/2}}{\Delta x}$ and u^{n} represents the solution at time step n. Since this time integration method incurs $O(\Delta t^{3})$ errors, the time step is chosen to be $\Delta t=8\Delta x^{5/3}$ in order that the error for the overall scheme is a measure of the spatial convergence only.

The norm of the error is computed by comparison with the exact solution at time $t=2$ according to

$$L_{1}=\frac{2}{N_{x}}\sum_{i=0}^{N_{x}}|u_{i}-u_{\text{exact},i}|, \tag{53a}$$

$$L_{2}=\sqrt{\frac{2}{N_{x}}\sum_{i=0}^{N_{x}}(u_{i}-u_{\text{exact},i})^{2}}, \tag{53b}$$

$$L_{\infty}=\max|u_{i}-u_{\text{exact},i}|\quad\text{for } i=0,\ldots,N_{x}, \tag{53c}$$

where $N_x + 1$ is the number of grid points in the domain $[-1, 1]$. Note that $N_x = 2/\Delta x$. These errors for various values of Δx are given in Tables 5–8 as well as the order of convergence between each level of resolution.

Table 5 shows the results for the upstream central scheme. This scheme, which gives optimal results for a five point stencil, is seen to converge at fifth order. Comparison of the errors given in Tables 5 and 6 illustrates how well the WENO5M scheme is able to mimic the upstream central scheme, even in the presence of critical points where $f''' \neq 0$ and where ϵ is small. The WENO5M scheme is also seen to converge at fifth order.

Table 5
Convergence properties of upstream central scheme

Δx	L_1		L_2		L_∞	
	r_c	Norm	r_c	Norm	r_c	Norm
4.00×10^{-2}	–	1.45316×10^{-3}	–	1.29424×10^{-3}	–	1.80818×10^{-3}
2.00×10^{-2}	5.02392	4.46646×10^{-5}	5.00981	4.01709×10^{-5}	4.99935	5.65313×10^{-5}
1.00×10^{-2}	5.01324	1.38302×10^{-6}	5.01072	1.24605×10^{-6}	5.01194	1.75205×10^{-6}
5.00×10^{-3}	5.00261	4.31411×10^{-8}	5.00225	3.88783×10^{-8}	5.00254	5.46551×10^{-8}
2.50×10^{-3}	5.00179	1.34649×10^{-9}	5.00173	1.21349×10^{-9}	5.00193	1.70569×10^{-9}
1.25×10^{-3}	5.00053	4.20624×10^{-11}	5.00052	3.79078×10^{-11}	5.00062	5.32799×10^{-11}
6.25×10^{-4}	5.00010	1.31436×10^{-12}	5.00010	1.18454×10^{-12}	5.00014	1.66483×10^{-12}
3.12×10^{-4}	5.00000	4.10738×10^{-14}	5.00000	3.70169×10^{-14}	5.00002	5.20253×10^{-14}

Table 6
Convergence properties of WENO5M ($\epsilon = 10^{-40}$)

Δx	L_1		L_2		L_∞	
	r_c	Norm	r_c	Norm	r_c	Norm
4.00×10^{-2}	–	1.45252×10^{-3}	–	1.29382×10^{-3}	–	1.80832×10^{-3}
2.00×10^{-2}	5.02322	4.46665×10^{-5}	5.00941	4.01691×10^{-5}	4.99951	5.65292×10^{-5}
1.00×10^{-2}	5.01330	1.38302×10^{-6}	5.01066	1.24604×10^{-6}	5.01188	1.75205×10^{-6}
5.00×10^{-3}	5.00261	4.31411×10^{-8}	5.00224	3.88783×10^{-8}	5.00255	5.46551×10^{-8}
2.50×10^{-3}	5.00179	1.34649×10^{-9}	5.00173	1.21349×10^{-9}	5.00193	1.70569×10^{-9}
1.25×10^{-3}	5.00053	4.20624×10^{-11}	5.00052	3.79078×10^{-11}	5.00062	5.32799×10^{-11}
6.25×10^{-4}	5.00010	1.31436×10^{-12}	5.00010	1.18454×10^{-12}	5.00014	1.66483×10^{-12}
3.12×10^{-4}	5.00000	4.10738×10^{-14}	5.00000	3.70169×10^{-14}	5.00002	5.20253×10^{-14}

Table 7
Convergence properties of WENO5 ($\epsilon = 10^{-6}$) as implemented in [1]

Δx	L_1		L_2		L_∞	
	r_c	Norm	r_c	Norm	r_c	Norm
4.00×10^{-2}	–	1.57063×10^{-3}	–	1.36967×10^{-3}	–	1.96666×10^{-3}
2.00×10^{-2}	4.93920	5.11949×10^{-5}	4.93272	4.48456×10^{-5}	5.00709	6.11565×10^{-5}
1.00×10^{-2}	4.94455	1.66252×10^{-6}	4.84158	1.56408×10^{-6}	4.02856	3.74736×10^{-6}
5.00×10^{-3}	5.03706	5.06362×10^{-8}	4.99207	4.91468×10^{-8}	4.72751	1.41450×10^{-7}
2.50×10^{-3}	5.06115	1.51671×10^{-9}	5.18207	1.35375×10^{-9}	6.12173	2.03132×10^{-9}
1.25×10^{-3}	5.04054	4.60838×10^{-11}	5.05252	4.07921×10^{-11}	5.14205	5.75264×10^{-11}
6.25×10^{-4}	5.04409	1.39677×10^{-12}	5.02493	1.25292×10^{-12}	5.01446	1.77977×10^{-12}
3.12×10^{-4}	5.03707	4.25417×10^{-14}	5.02796	3.84020×10^{-14}	5.03535	5.42717×10^{-14}

Table 8
Convergence properties of WENO5 ($\epsilon = 10^{-40}$) as implemented in [1]

Δx	L_1		L_2		L_∞	
	r_c	Norm	r_c	Norm	r_c	Norm
4.00×10^{-2}	–	1.57063×10^{-3}	–	1.36964×10^{-3}	–	1.96669×10^{-3}
2.00×10^{-2}	4.93832	5.12262×10^{-5}	4.93107	4.48960×10^{-5}	5.00736	6.11465×10^{-5}
1.00×10^{-2}	4.90103	1.71450×10^{-6}	4.77077	1.64461×10^{-6}	3.81337	4.34944×10^{-6}
5.00×10^{-3}	4.70139	6.58987×10^{-8}	4.28898	8.41301×10^{-8}	3.39847	4.12469×10^{-7}
2.50×10^{-3}	4.57542	2.76401×10^{-9}	3.84598	5.85055×10^{-9}	3.29195	4.21128×10^{-8}
1.25×10^{-3}	4.42426	1.28737×10^{-10}	3.70724	4.47926×10^{-10}	3.26545	4.37942×10^{-9}
6.25×10^{-4}	4.30740	6.50202×10^{-12}	3.68715	3.47748×10^{-11}	3.26639	4.55131×10^{-10}
3.12×10^{-4}	4.22130	3.48587×10^{-13}	3.68948	2.69539×10^{-12}	3.27135	4.71371×10^{-11}

Comparison of the results reported in Table 5 with those of Tables 7 and 8 also reveals some interesting features of the WENO5 scheme. Table 7 shows that the order of convergence for $\epsilon = 10^{-6}$ fluctuates around fifth order. The error incurred at this level of grid refinement by using WENO5 with $\epsilon = 10^{-40}$ is much worse; in fact, the error is third order in the L_∞ norm as seen in Table 8.

The overall L_∞ convergence behavior of these schemes is seen in Fig. 7. Predictions given by the central and WENO5M schemes are indistinguishable at the scale shown. Both of these solution sets converge at fifth order as evidenced by the slope of these two lines. For WENO5, the convergence rate is seen to vary with ϵ and Δx. WENO5 with $\epsilon = 10^{-16}$ is seen to converge consistently at third order. This third-order convergence line along with the fifth-order convergence line of the upstream central scheme form an envelope which contains the other WENO5 cases. All the other WENO5 cases are seen to peal away from the third-order line and asymptotically approach the fifth-order upstream central case. This is due to the gradual domination of ϵ over the β_k as Δx is decreased. Note that the slope of the various WENO5 schemes are

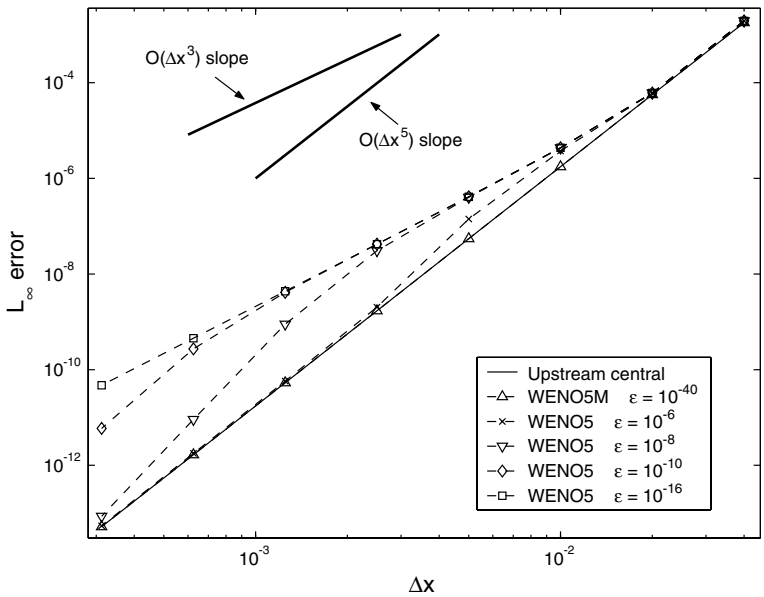

Fig. 7. Convergence plot for $(\partial u/\partial t + \partial u/\partial x) = 0$ with the initial condition $u(x, t = 0) = \sin(\pi x - \frac{\sin(\pi x)}{\pi})$ for $x \in [-1,1]$ with periodic boundary conditions. In each case $\Delta t = 8\Delta x^{5/3}$.

seen to be greater than fifth order as ϵ begins to dominate. This explains the "super-convergence" phenomenon in which the WENO5 schemes converge at higher than fifth order for some grid resolutions. Even so, these schemes are never more accurate than the fifth-order upstream central scheme.

5.4. Euler example I: shock entropy wave interaction

For the one-dimensional Euler equations of gas dynamics, we have the conservation of mass, momentum and energy:

$$\begin{aligned}
&\frac{\partial \rho}{\partial t} + \frac{\partial(\rho u)}{\partial x} = 0,\\
&\frac{\partial(\rho u)}{\partial t} + \frac{\partial(\rho u^2 + p)}{\partial x} = 0,\\
&\frac{\partial E}{\partial t} + \frac{\partial(uE + up)}{\partial x} = 0,
\end{aligned} \tag{54}$$

where ρ, u, p and E are the density, particle velocity, pressure and total energy, respectively. The system of equations is closed by specifying an equation of state; here, the calorically perfect ideal gas equation of state is used:

$$E = p(\gamma - 1) + \tfrac{1}{2}\rho u^2. \tag{55}$$

For the shock entropy wave interaction problem [7], $\gamma = 1.4$ and the initial conditions are set by a Mach 3 shock interacting with a perturbed density field:

$$(\rho, u, p) = \begin{cases} (\frac{27}{7}, \frac{4\sqrt{35}}{9}, \frac{31}{3}) & \text{if } x < -4,\\ (1 + \frac{1}{5}\sin 5x, 0, 1) & \text{if } x \geqslant -4 \end{cases} \tag{56}$$

with zero-gradient boundary conditions at $x = \pm 5$.

The Roe scheme is used for calculating the fluxes in the system of hyperbolic conservation laws [7] and the third-order Runge–Kutta scheme of Eq. (52) is used to advance in time. Other schemes, such as non-decomposition based Lax–Friedrichs schemes [14,15], have been utilized with similar results. The solutions at $t = 1.8$ for the Roe scheme are given in Figs. 8 and 9 for the WENO5 ($\epsilon = 10^{-6}$) and WENO5M ($\epsilon = 10^{-40}$) schemes, respectively. Each was computed using $N_x = N_t = 400$, where N_t is the number of time steps. It is clear, even though the formal rate of convergence is no better than first order due to the captured shocks, that the WENO5M scheme resolves the salient features of the flow with higher fidelity. This is particularly true at points in the flow where the solution's first derivative vanishes.

5.5. Euler example II: interacting blast waves

The interacting blast wave example [16] is another difficult test of shock capturing schemes. The Euler equation (55) with $\gamma = 1.4$ are solved with initial conditions

$$(\rho, u, p) = \begin{cases} (1, 0, 1000) & \text{if } 0 \leqslant x < 0.1,\\ (1, 0, 0.01) & \text{if } 0.1 \leqslant x < 0.9,\\ (1, 0, 100) & \text{if } 0.9 \leqslant x \leqslant 1, \end{cases} \tag{57}$$

with reflection boundary conditions at $x = 0$ and $x = 1$.

Again, the Roe scheme and third-order Runge–Kutta are used in constructing the numerical solution. The solutions at $t = 0.038$ are given in Figs. 10 and 11 for the WENO5 ($\epsilon = 10^{-6}$) and WENO5M

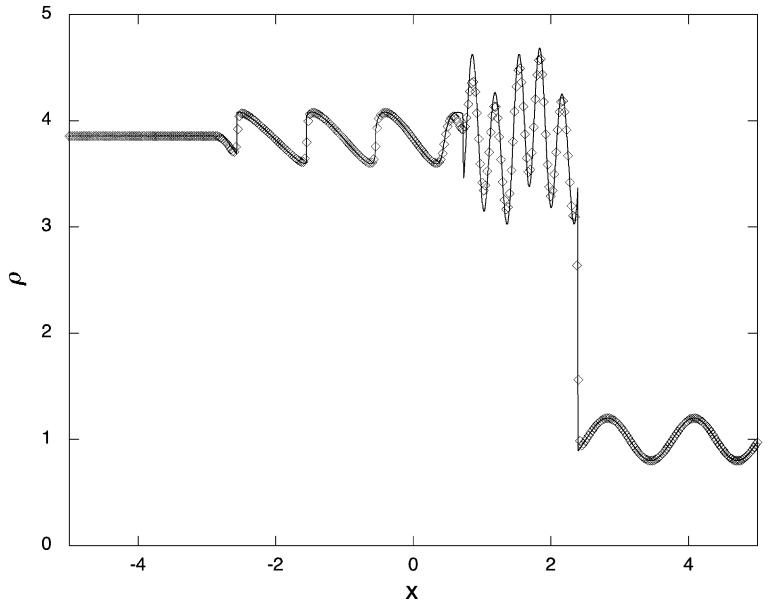

Fig. 8. Shock entropy wave interaction. Density plot of WENO5 ($\epsilon = 10^{-6}$) solution at $t = 1.8$ with $N_x = N_t = 400$, $\diamond$, and well-resolved WENO5M ($\epsilon = 10^{-40}$) solution with $N_x = N_t = 12{,}800$, solid line.

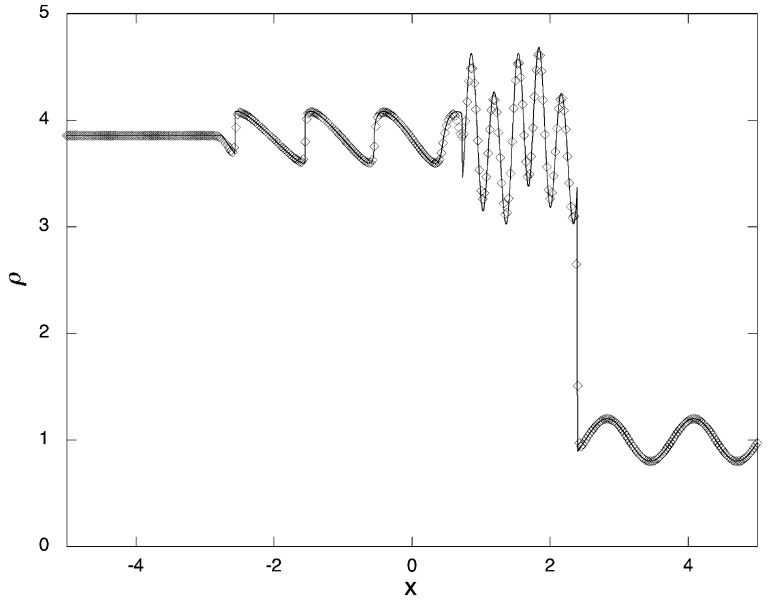

Fig. 9. Shock entropy wave interaction. Density plot of WENO5M ($\epsilon = 10^{-40}$) solution at $t = 1.8$ with $N_x = N_t = 400$, $\diamond$, and well-resolved WENO5M ($\epsilon = 10^{-40}$) solution with $N_x = N_t = 12{,}800$, solid line.

($\epsilon = 10^{-40}$) schemes, respectively. Each was computed using $N_x = 400$ and $N_t = 800$. Careful examination reveals that the WENO5M scheme resolves the salient features of the flow with higher fidelity. The three contact waves, near $x = 0.595, 0.765, 0.799$, are better resolved as too are the various peaks and valleys.

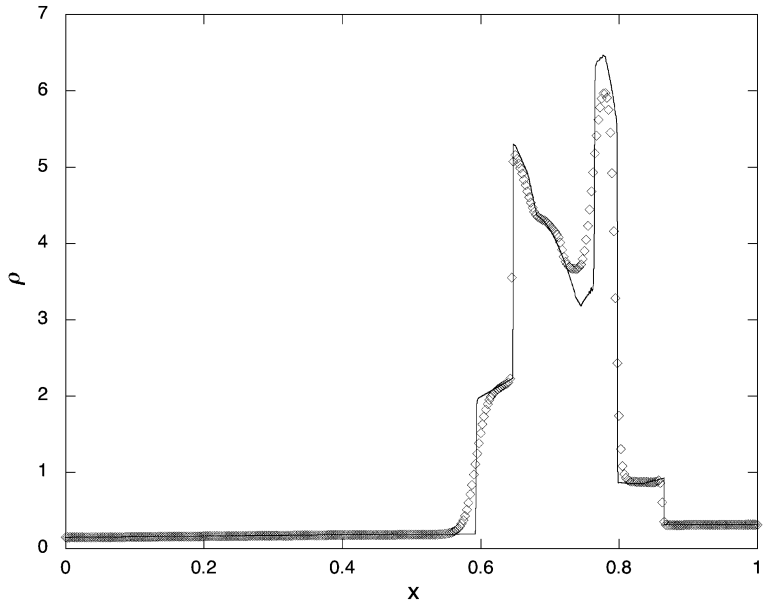

Fig. 10. Interacting blast waves. Density plot of WENO5 ($\epsilon = 10^{-6}$) solution at $t = 0.038$ with $N_x = 400$, $N_t = 800$, $\diamond$, and well-resolved WENO5M ($\epsilon = 10^{-40}$) solution with $N_x = 12{,}800$, $N_t = 25{,}600$, solid line.

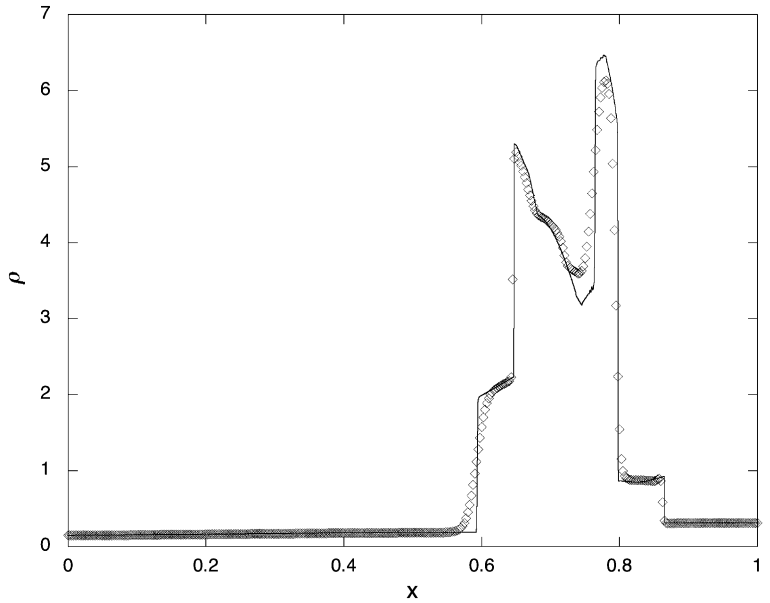

Fig. 11. Interacting blast waves. Density plot of WENO5M ($\epsilon = 10^{-40}$) solution at $t = 0.038$ with $N_x = 400$, $N_t = 800$, $\diamond$, and well-resolved WENO5M ($\epsilon = 10^{-40}$) solution with $N_x = 12{,}800$, $N_t = 25{,}600$, solid line.

5.6. Euler example III: Riemann problem of lax

The Riemann problem of Lax [17] was simulated with both the WENO5 and WENO5M methods. The initial conditions are:

$$(\rho, u, p) = \begin{cases} (0.445, 0.698, 3.528) & \text{if } x \leqslant 0, \\ (0.5, 0, 0.571) & \text{if } x > 0 \end{cases} \tag{58}$$

with zero gradient boundary conditions at $x = \pm 0.5$. The solution was integrated to $t = 0.13$ with the Roe scheme and third-order Runge–Kutta. For $N_t = N_x = 100$, Fig. 12 demonstrates the improved resolution ability of the present method, while still maintaining the ENO property.

5.7. Euler example IV: Riemann problem of sod

Lastly, the standard shock tube problem of Sod [12] was simulated with both the WENO5 and WENO5M methods, and the grid was refined so as to enable determination of the convergence rates. The initial conditions are:

$$(\rho, u, p) = \begin{cases} (1, 0, 1) & \text{if } x \leqslant 0, \\ (0.125, 0, 0.1) & \text{if } x > 0 \end{cases} \tag{59}$$

with zero gradient boundary conditions at $x = \pm 0.5$. The solution was integrated to $t = 0.14385$ with the Roe scheme and third-order Runge–Kutta. The results of the convergence study, with $N_t = N_x$, are summarized in Table 9. Both methods predict qualitatively similar results, but the WENO5M method consistently predicts solutions with roughly 10% less error than the WENO5 method, similar to Fig. 12. The rate of convergence of both are roughly 5/6 order as $\Delta x \to 0$. This convergence rate, at or below first order,

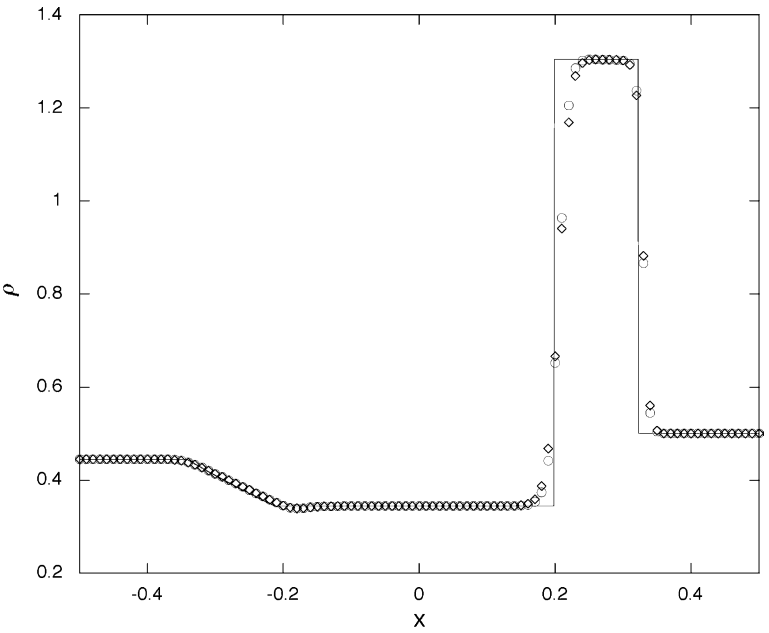

Fig. 12. Riemann problem of Lax [17]. Density plot of WENO5 ($\epsilon = 10^{-6}$) solution at $t = 0.13$ with $N_x = N_t = 100$, ◇; WENO5M ($\epsilon = 10^{-40}$) solution with $N_x = N_t = 100$, ○; Exact solution, solid line.

Table 9
L_1 density error norms and convergence rates, r_c, for WENO5 ($\epsilon = 10^{-6}$) as implemented in Ref. [1] and WENO5M ($\epsilon = 10^{-40}$) methods applied to Sod's [12] shock tube problem

Δx	L_1		r_c	
	WENO5	WENO5M	WENO5	WENO5M
1/100	6.88×10^{-3}	6.35×10^{-3}	–	–
1/200	3.67×10^{-3}	3.34×10^{-3}	0.907	0.925
1/400	2.01×10^{-3}	1.84×10^{-3}	0.866	0.860
1/800	1.03×10^{-3}	9.37×10^{-4}	0.970	0.975
1/1600	5.11×10^{-4}	4.59×10^{-4}	1.008	1.030
1/3200	2.76×10^{-4}	2.48×10^{-4}	0.889	0.885
1/6400	1.38×10^{-4}	1.23×10^{-4}	0.998	1.018
1/12800	7.27×10^{-5}	6.40×10^{-5}	0.927	0.938
1/25600	3.89×10^{-5}	3.42×10^{-5}	0.900	0.906
1/51200	2.18×10^{-5}	1.91×10^{-5}	0.837	0.837
1/102400	1.20×10^{-5}	1.09×10^{-5}	0.858	0.817

is characteristic of all shock capturing schemes when applied to flows with embedded discontinuities. In particular, nominally fifth-order shock capturing algorithms converge at roughly 5/6 order in the L_1 norm for discontinuities in linearly degenerate fields [18]. This is commensurate with the notion that a captured linear discontinuity will smear over a number of computational zones proportional to $N_x^{1/(r_c+1)}$, where r_c is the nominal order of the scheme [19].

6. Summary of WENO and mapped WENO schemes of 3rd to 11th order

WENO schemes (and their monotonicity-preserving counterparts) up to 11th order have been outlined in [9]. Notationally, let n_{CP} denote the order of the critical point. For example $n_{CP} = 0$ corresponds to $f' \neq 0$; $n_{CP} = 1$ corresponds to $f' = 0$, $f'' \neq 0$; $n_{CP} = 2$ corresponds to $f' = 0$, $f'' = 0$, $f''' \neq 0$, etc.

As with the fifth-order WENO scheme, the detailed Taylor series analysis of these higher order WENO schemes can be performed, under the assumption $\epsilon = 0$. It is easily verified that away from critical points, the schemes are $(2r-1)$th order accurate as advertised, but all of the schemes drop by 2 orders at points near $n_{CP} = 1$. For each further increase in n_{CP}, the schemes continue to degrade by an order of accuracy, until the schemes are only $(r-1)$th order accurate. Inferring from the results, it is found that the rate of convergence can be related to r and n_{CP} in the following manner (at least for $r \leqslant 6$):

$$r_c = \begin{cases} 2r-1 & \text{if not near a critical point,} \\ \max(2r-2-n_{CP}, n_{CP}) & \text{otherwise.} \end{cases} \tag{60}$$

Note that once $n_{CP} > r-1$, the rate of convergence actually starts to increase. This is simply due to the fact that the function is so flat that any consistent scheme will yield better convergence locally (for example, a first-order scheme, $r = 1$, is actually second-order accurate at $x = 0$ for the cubic function $f(x) = x^3$, i.e. $n_{CP} = 2$).

Table 10 demonstrates the convergence rates for the WENO schemes of $r = 2, 3, 4, 5, 6$, corresponding to Eq. (60). Also shown are the rates of convergence for the mapped WENO schemes, with either 1 or 2 applications of Eq. (44) followed by Eq. (46). Note that for $n_{CP} = r-1$, the individual weights are O(1) away from being the ideal weights, and thus the mappings are ineffective. At these points, it is difficult for any scheme to distinguish the difference between a discontinuity and a function that is nearly flat but relatively rapidly changing on the grid. For the cases where $1 \leqslant n_{CP} < r-1$, it is predicted that the mapped WENO schemes can recover optimal convergence rates.

Table 10
Rates of convergence, r_c, for WENO and mapped WENO schemes as a function of critical point order

	n_{CP}	r_c-WENO	r_c-WENO-1 mapping	r_c-WENO-2 mappings
$r = 2$	0	3	3	3
	1	1	1	1
$r = 3$	0	5	5	5
	1	3	5	5
	2	2	2	2
$r = 4$	0	7	7	7
	1	5	7	7
	2	4	6	7
	3	3	3	3
$r = 5$	0	9	9	9
	1	7	9	9
	2	6	9	9
	3	5	7	9
	4	4	4	4
$r = 6$	0	11	11	11
	1	9	11	11
	2	8	11	11
	3	7	11	11
	4	6	8	11
	5	5	5	5

7. Conclusion

It has been shown that the previously published constraints for fifth-order accurate WENO schemes are incomplete. The extensions to higher orders are similarly afflicted near critical points. Former algorithms for finding these weights do not satisfy this incomplete set of criteria in the neighborhood of critical points and, in the worst case, result in $(r-1)$th order convergence for smooth flows. Furthermore, an explanation has been given of the dramatic effect that ϵ, in conjunction with the level of grid resolution, has on the convergence of WENO5 schemes. A correction is given which achieves the full $(2r-1)$th order accuracy in the neighborhood of critical points where $f' = 0$, even for very small ϵ.

Lastly, while it is clear that the improvement described here allows true fifth-order convergence rates and consequent high accuracy to be realized when approximating smooth solutions, the improvement in accuracy is more modest when flows with embedded discontinuities are considered. Certainly for such flows, side by side comparisons reveal that the predictions of WENO5M are better than those of WENO5. However, in both cases the rate of convergence dramatically drops to no more than first order. Consequently, the improvement for flows with shocks is proportional rather than geometric. While this is often recognized in much of the computational literature, it is as often unrecognized; the enthusiasm displayed by some advocates of high order methods for problems with shocks should be proportionately tempered.

References

[1] G.-S. Jiang, C.-W. Shu, Efficient implementation of weighted ENO schemes, J. Comput. Phys. 126 (1996) 202–228.
[2] A. Harten, High resolution schemes for hyperbolic conservation laws, J. Comput. Phys. 49 (1983) 357–393.
[3] B. Van Leer, Towards the ultimate conservative difference scheme II, monotonicity and conservation combined in a second order scheme, J. Comput. Phys. 14 (1974) 361–470.

[4] B. Van Leer, Towards the ultimate conservative difference scheme V, a second order sequel to Godunov's method, J. Comput. Phys. 32 (1979) 101–136.
[5] A. Harten, B. Enquist, S. Osher, S. Chakravarthy, Uniformly high order accurate essentially non-oscillatory schemes III, J. Comput. Phys. 71 (1987) 231–303.
[6] C.-W. Shu, S. Osher, Efficient implementation of essentially non-oscillatory shock-capturing schemes, J. Comput. Phys. 77 (1988) 439–471.
[7] C.-W. Shu, S. Osher, Efficient implementation of essentially non-oscillatory shock-capturing schemes II, J. Comput. Phys. 83 (1989) 32–78.
[8] X.-D. Liu, S. Osher, T. Chan, Weighted essentially non-oscillatory schemes, J. Comput. Phys. 115 (1994) 200–212.
[9] D.S. Balsara, C.-W. Shu, Monotonicity preserving weighted essentially non-oscillatory schemes with increasingly high order of accuracy, J. Comput. Phys. 160 (2000) 405–452.
[10] R. Fedkiw, Simplified discretization of systems of hyperbolic conservation laws containing advection equations, J. Comput. Phys. 157 (2000) 302–326.
[11] S. Osher, R. Fedkiw, Level Set Methods and Dynamic Implicit Surfaces, Applied Mathematical Sciences, vol. 152, Springer, New York, 2003, p. 154.
[12] G.A. Sod, Survey of several finite-difference methods for systems of non-linear hyperbolic conservation laws, J. Comput. Phys. 27 (1978) 1–31.
[13] IEEE Standards Board, IEEE Standard for Binary Floating-Point Arithmetic, IEEE Standard 754-1985, 1985.
[14] S. Xu, T. Aslam, D.S. Stewart, High resolution numerical simulation of ideal and non-ideal compressible reacting flows with embedded internal boundaries, Combust. Theory Model. 1 (1) (1997) 113–142.
[15] X.-D. Liu, S. Osher, Convex ENO high order multi-dimensional schemes without field-by-field decomposition or staggered grids, J. Comput. Phys. 142 (1998) 304–330.
[16] P. Woodward, P. Colella, The numerical simulation of two-dimensional fluid flow with strong shocks, J. Comput. Phys. 54 (1984) 115–173.
[17] P.D. Lax, Weak solutions of nonlinear hyperbolic equations and their numerical computation, Comm. Pure Appl. Math. 7 (1954) 159–193.
[18] T.D. Aslam, A level set algorithm for tracking discontinuities in hyperbolic conservation laws I: scalar equations, J. Comput. Phys. 167 (2001) 413–438.
[19] R. Donat, S. Osher, Propagation of error into regions of smoothness for non-linear approximations to hyperbolic equations, Comput. Meth. Appl. Mech. Eng. 80 (1990) 59–64.